This is the accepted manuscript made available via CHORUS. The article has been published as:

Confinement of many-body Bethe strings

Jiahao Yang, Tao Xie, S. E. Nikitin, Jianda Wu, and A. Podlesnyak

Phys. Rev. B **108**, L020402 — Published 18 July 2023

DOI: 10.1103/PhysRevB.108.L020402

Confinement of many-body Bethe strings

Jiahao Yang,[1] Tao Xie,[2] S. E. Nikitin,[3,*] Jianda Wu,[1,4,5,†] and A. Podlesnyak[2]

[1] *Tsung-Dao Lee Institute, Shanghai Jiao Tong University, Shanghai 201210, China*
[2] *Neutron Scattering Division, Oak Ridge National Laboratory, Oak Ridge, TN 37831, USA*
[3] *Quantum Criticality and Dynamics Group, Paul Scherrer Institut, CH-5232 Villigen-PSI, Switzerland*
[4] *School of Physics and Astronomy, Shanghai Jiao Tong University, Shanghai 200240, China*
[5] *Shanghai Branch, Hefei National Laboratory, Shanghai 201315, China*

(Dated: April 21, 2023)

Based on Bethe-ansatz approach and inelastic neutron scattering experiments, we reveal evolution of confinement of many-body Bethe strings in ordered regions of quasi-one-dimensional antiferromagnet $YbAlO_3$. In the antiferromagnetic phase, the spin dynamics is dominated by the confined length-1 Bethe strings, whose dominancy in the high-energy branch of the excitation spectrum yields to the confined length-2 Bethe strings when the material is tuned to the spin-density-wave phase. In the thermal-induced disordered region, the confinement effect disappears, and the system restores the conventional quantum integrable physics of the one-dimensional Heisenberg model. Our results establish a unified picture based on Bethe string for the spin dynamics in different magnetic phases of $YbAlO_3$, and thus provide profound insight into the many-body quantum magnetism.

Introduction. The one-dimensional (1D) spin-1/2 Heisenberg model, a paradigmatic model for studying quantum many-body physics, exhibits rich magnetic excitations such as magnon [1–3], spinon [4–8], (anti)psinon [9], and Bethe strings [10–19]. Though the former three types of excitations have been well studied via both theory and experiments, the Bethe strings, exotic many-magnon bound states, are long-sought in real materials. Recently, with the aid of Bethe-ansatz calculation [15], substantial progress has been made by THz spectroscopy and inelastic neutron scattering (INS) experiments on the quasi-1D Heisenberg-Ising antiferromagnet $SrCo_2V_2O_8$ (SCVO) [16, 18] and $BaCo_2V_2O_8$ (BCVO) [17]. The progress reveals the existence of the Bethe strings in SCVO and BCVO and identifies their vital contributions to spin dynamics.

Recently, a rare-earth-based material, $YbAlO_3$ (YAO), is evidenced to be a quasi-1D Heisenberg antiferromagnet [20, 21]. The magnetic ion Yb^{3+} carries on an effective spin $S = 1/2$ due to the combined effect between the spin-orbit coupling and the crystal field effect. And among Yb^{3+} ions, the dominant spin exchange interaction (J) is isotropic along the chain direction (the c direction in Fig. 1**a**) [20, 22]. The Tomonaga-Luttinger liquid (TLL) theory has been successfully applied to understand ground state and low-energy excitations of the material but failed to explain the physics for the observed spectrum with rich structure beyond low-energy region [20, 22]. Thus a unified physical picture beyond TLL is desired to give a complete understanding for the complete spectral response.

In this letter by the combined efforts of the INS experiment and the Bethe-ansatz calculations, we report that the Bethe strings can provide a unified physical picture to give a full understanding for all spin dynamical spectra observed in different regions of YAO. Specifically, in ordered regions, the confined length-1 strings dominate the dynamic spectrum in the antiferromagnetic (AFM) phase, which gives way to the confined length-2 strings for the high energy branch of the spin dynamic when the material turns into the spin-density-wave (SDW) phase. In the thermal-induced disordered region Bethe strings are released from confinement. Our work not only uncovers the existence and confinement of Bethe strings but also provides a unified picture based on Bethe string to quantitatively describe the spin dynamics in different phases of YAO, which is beyond the conventional static order-parameter paradigm [23] and low-energy effective theories [20, 22, 24–28].

Experimental details. The inelastic neutron scattering (INS) experiments were performed at the time-of-flight Cold Neutron Chopper Spectrometer (CNCS) [29, 30] at the Spallation Neutron Source, Oak Ridge National Laboratory. A YAO crystal used in previous studies [20, 22] with a mass of ~ 0.5 g was mounted in the $(0\ K\ L)$ scattering plane. The zero field data were collected in a standard cryostat equipped with a dilution insert. The 0.4 T dataset was measured in a vertical 5 T cryomagnet with a dilution refrigerator and field was applied along the [1 0 0] direction (the easy axis). To obtain optimal coverage in the energy and momentum space, the sample was rotated along the vertical axis by 90°. The data were collected with an incident neutron energy $E_\mathrm{i} = 1.55$ meV, with an energy resolution of 0.05 meV at the elastic line. We used the software packages MantidPlot [31] and Horace [32] for data reduction and analysis. The actual temperature of the sample was calculated using the detailed balance principle, $S(\mathbf{Q}, E) = e^{-E/k_\mathrm{B}T} S(\mathbf{Q}, -E)$, by comparing the spectral intensity at positive and negative energy transfer.

Theoretical Models. The phase diagram of YAO (Fig. 1**b**) is obtained from specific heat and magnetization measurements [20, 22, 23], which is qualitatively similar to that of SCVO [18] and BCVO [33]. At low temper-

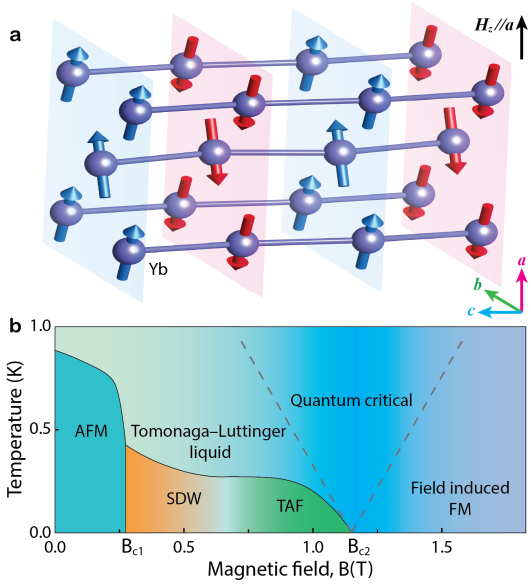

FIG. 1. Schematic illustration of the magnetic structure and phase diagram of $YbAlO_3$. **a** Below Néel temperature T_N, the magnetic moments of Yb ions are antiferromagnetically (AFM) ordered along chain direction (the c-axis), and the interchain coupling is ferromagnetic (FM) in the ab-plane. **b** Field-temperature phase diagram with AFM phase, spin-density-wave (SDW) phase, and presumably transverse-antiferromagnetic (TAF) phase, indicated by blue, orange, and green, respectively. Two gray dotted lines show the crossover regions between Tomonaga-Luttinger liquid, quantum critical, and field-induced FM.

atures, the interchain coupling helps to stabilize different long-range orders (LROs) in the material. By tuning the external magnetic field, the material can change from the AFM phase to the SDW phase after crossing through the critical field $B_{c1} = 0.32$ T. With the field further increasing to about 0.7 T the system begins to transform from the SDW phase to the presumably transverse-antiferromagnetic (TAF) phase and eventually is fully polarized when $B > B_{c2} = 1.15$ T. In the disordered region of YAO, the interchain coupling can be neglected following the chain mean-field treatment, and the dominant magnetic property in YAO can then be described by the spin-1/2 Heisenberg model with external longitudinal field H_z (along a direction in Fig. 1**a**),

$$H_0 = J \sum_i \mathbf{S}_i \cdot \mathbf{S}_{i+1} - H_z S_i^z, \tag{1}$$

where the AFM coupling $J = 0.21$ meV, and $\mathbf{S}_i$ is the spin operator at site i with spin components S_i^α ($\alpha = x, y, z$). In the ordered phases, different LROs are characterized by different ordering wavevector $Q = (1-m)\pi$ where magnetization density m is the ratio of magnetization M_z to its saturation value M_s. The LRO can effectively induce a mean field $\mathbf{h}_z = h_Q \sum_i \cos(Qr_i)\hat{z}$ which

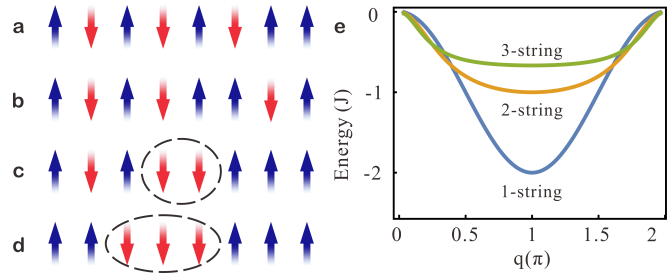

FIG. 2. Pictorial spin configurations for different quasiparticles of 1D spin-1/2 Heisenberg model and their band structures. **a**, Ground state (GS) with SDW ordering and finite magnetization $M_z = N/2 - M$, where M is the number of down spins with respect to the fully up-polarized state. **b-d**, Excitations generated from the GS. Psinon-antipsinon pair $\psi\psi^*$ (**b**), two-string χ^2 (**c**), and three string χ^3 (**d**). Viewing the down spin (red arrow) and up spin (blue arrow) as the magnon and vacuum respectively, many-body Bethe string χ^j ($j \geq 2$) contains j bounded magnons and lives in the corresponding j-string band in **e**. The 1-string band accommodates unbound magnons, and GS has the lowest total energy in the 1-string band.

couples to the spin chain Eq. (1) [20, 22, 27, 28],

$$H = H_0 - h_Q \sum_i \cos(Qr_i) S_i^z, \tag{2}$$

where field strength h_Q is generally dependent on the strength of LRO. Apart from the AFM phase, the effective mean field $\mathbf{h}_z$ in general is incommensurate, and becomes commensurate when $2\pi/Q$ is a rational number (for example, $\mathbf{h}_z$ is commensurate in AFM phase with $Q = \pi$). In this letter, following Bethe ansatz approach we analytically study the spin dynamics based on the effective Hamiltonians of Eq. (1) and Eq. (2) for disordered and ordered regions, respectively. The obtained results are then compared in detail with the INS results, which reveals rich spin dynamics as discussed below. Note, due to the strong Ising-anisotropy of g tensor in YAO the main contribution to the INS spectrum comes from the longitudinal spin component [20], which makes interpretation of the spectral function much easier compared with BCVO and SCVO with more isotropic g factor of the ground state doublet.

Dynamical structure factor. Following standard linear response theory [34–36], the thermal dynamical structure factor (DSF) for spin along longitudinal (z) direction is given by ($k_B = 1$)

$$S^{zz}(T, q, \omega) = \frac{2\pi}{\mathcal{Z}} \sum_{\lambda,\mu} e^{-E_\lambda/T} |\langle\lambda|S_q^z|\mu\rangle|^2 \delta(\hbar\omega - E_\mu + E_\lambda), \tag{3}$$

with partition function $\mathcal{Z}$, transfer momentum q and transfer energy $\hbar\omega$ between two eigenstates $|\lambda\rangle$ and $|\mu\rangle$ with eigenenergies E_λ and E_μ. The double summation goes over all the eigenstates of the effective Hamiltonians

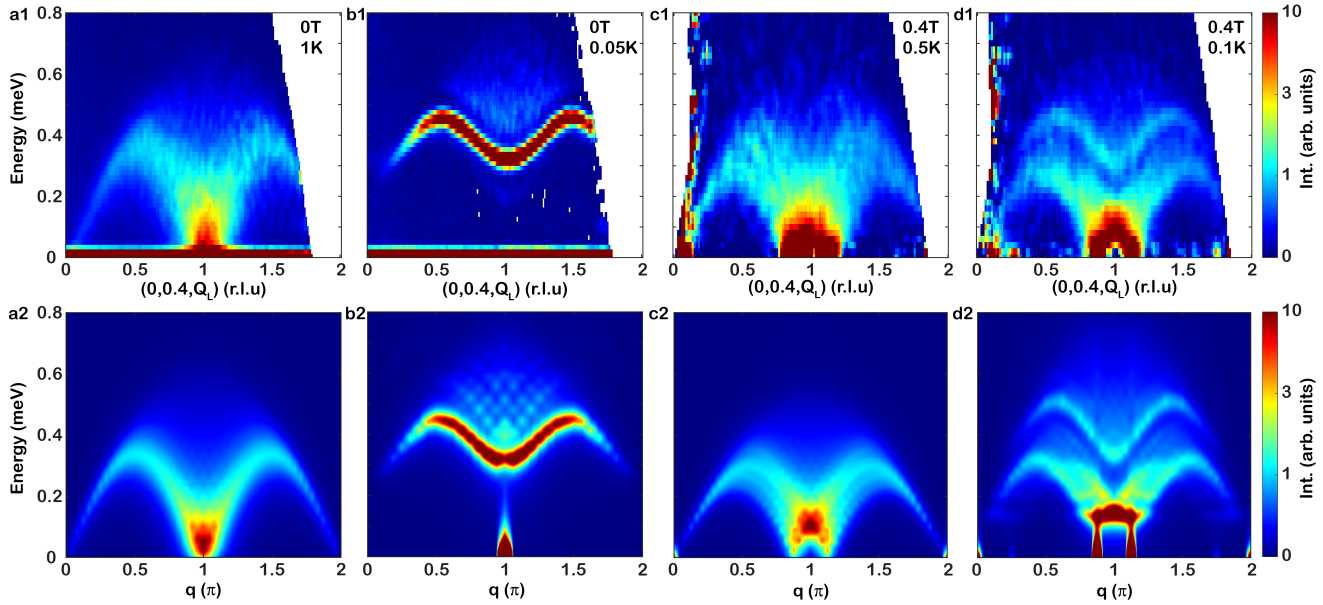

FIG. 3. Spin dynamics for YAO. INS spectra without magnetic fields were collected at 1 K (**a1**) and 0.05 K (**b1**). The data in (**a1**) and (**b1**) were integrated within $K = [0.3, 0.5]$, $H = [-0.1, 0.1]$ r.l.u.. No background subtraction was applied to the data. The INS spectra at $B = 0.4$ T at 0.5 K (**c1**) and 0.1 K (**d1**). The data were integrated within all available $\mathbf{Q}$ ranges along the orthogonal directions and the background measured at 3 T was subtracted from both spectra. Correspondingly, thermal DSFs of H_0 are determined in **a2** and **c2**, and zero temperature DSFs of H are determined in **b2** and **d2** where the ordering fields are $h_\pi = 0.27J$ and $h_Q = 0.35J$ respectively.

of Eq. (1) or Eq. (2). At zero temperature the system is in the ground state, i.e. $|\lambda\rangle = |GS\rangle$, and the thermal DSF reduces to a single summation,

$$S^{zz}(q,\omega) = 2\pi \sum_{\mu} |\langle GS|S^z_q|\mu\rangle|^2 \delta(\hbar\omega - E_\mu + E_{GS}). \quad (4)$$

In the following, we focus on the transfer energy range $\hbar\omega \leq 0.8$ meV in compliance with the experimental data.

Analysis and Discussions. For the effective Hamiltonian H_0 of YAO, its excitations can be exactly obtained from the Bethe-ansatz method [37]. In general, the excitation can be decomposed into Bethe strings with different lengths. Typically, a Bethe string χ^j ($j \geq 2$) of length j contains j bounded magnons, referred to as j-string. While if $j = 1$, the 1-string χ^1 is just unbound magnon, as shown in Fig. 2. The psinon (ψ) and antipsinon (ψ^*) can be understood as the "particle" and "hole" excitations from the ground state in the 1-string band, which are always created in pairs ($\psi\psi^* s$). And the psinon-antipsinon (PAP) pairs can adiabatically connect to fractionalized fermionic spinons at $m = 0$ and bosonic magnons at $m \simeq 1$ [9]. All the excitations can be regarded as the combination of these quasiparticles, i.e. $n\chi^j n'\psi\psi^*$ with integers n, $n' \geq 0$. The obtained dynamical spectra can produce characteristic spectrum continua due to the many-body nature of Bethe states. Although the effective Hamiltonian H is different from H_0 by an effective field $\mathbf{h}_z$, it is beyond the integrability and can not be solved exactly. Here we tackle this problem by the truncated string state space method [38]. Following this method the thermal DSF is calculated to describe the data collected at 1 K and 0.5 K, while zero-temperature DSFs are obtained to compare with data at 0.05 K and 0.1 K.

In the disordered region with $B = 0$ T (corresponding to $m = 0$), the dominant low-energy excitations are 1-strings. When sample temperature $T_s = 1$ K $\sim 0.4J$, the thermal fluctuations are non-negligible and needs to be considered in the calculation. From thermal DSF Eq. (3) it is straightforward to observe that among thermal sampling states $|\lambda\rangle$ the spectral weight is exponentially suppressed with increasing eigenenergy E_λ due to the Boltzmann factor. As such it is reasonable to select a cutoff $E_\lambda \leq 4T_s$ for thermal sampling states $|\lambda\rangle$ (i.e. Boltzmann factor $\lesssim 1.8\%$). With $T_s = 1$ K and $m = 0$, the thermal DSF Eq. (3) of H_0 shows that 1-strings dominate the dynamical spectrum (Fig. 3**a2**) and exhibits a large thermal broadening effect compared with zero temperature result (see Supplemental Material [38]), and the INS spectrum (Fig. 3**a1**) agrees well with the theoretical spectrum (Fig. 3**a2**). In the AFM phase, the zero temperature DSF Eq. (4) of H with $h_\pi = 0.27J$ shows that 1-strings are confined by the effective staggered field and the corresponding INS spectrum (Fig. 3**b1**) is confirmed by the theoretical result (Fig. 3**b2**). Note that the Bragg peak at zero energy is present in our neutron scattering data at $\mathbf{Q} = (0\ 0\ 1)$, but not visible in Fig. 3**b2** because of the selected integration range, $K = [0.3, 0.5]$ r.l.u. It is

worth noting that spinon confinement observed in SCVO [39, 40], BCVO [41] and $CaCu_2O_3$ [42] is also the confinement of 1-strings. However, the spinon picture only works at $m = 0$ and is invalid when $m > 0$ [4–7], in contrast, the Bethe string picture can describe excitations for both of $m = 0$ and $m > 0$. Thus, we shall continuously discuss our results based on Bethe strings in the following.

In the disordered phase with $B = 0.4$ T (corresponding to $m \simeq 12\%$), 2-strings χ^2 are also favored in the spin dynamics in addition to 1-strings [19, 38]. When $T_s = 0.5$ K $\sim 0.2J$, the thermal fluctuation can not be neglected. Following the same strategy in the case of $T_s = 1$ K, thermal DSF Eq. (3) is determined for H_0 at T_s and $m \simeq 12\%$ with energy cutoff $E_\lambda \leq 4T_s$. In addition, with the presence of external field, the dipole interaction in ab plane would deviate from the "magic" line of vanishing dipole interaction [43], leading to non-negligible 3D fluctuations that further frustrate the intrachain couplings within the framework of the chain mean-field theory. From theoretical calculations, we find that at $B = 0.4$ T the obtained DSF with adjusted $J = 0.18$ meV (Fig. 3**c2**) is consistent with the INS experimental spectrum (Fig. 3**c1**). We note that the continuum of 2-strings is masked by that of 1-strings [38] and there is no clear energy gap between these two continua in Fig. 3**c1,c2**. In fact, this energy gap can be tuned by external magnetic field H_z, Ising-anisotropy of the Heisenberg-Ising model, and next-nearest-neighbor coupling J_2 in various DSFs. [15, 19, 44].

In the SDW phase with $B = 0.4$ T, the observed INS spectrum (Fig. 3**d1**) reveals rich structures of string excitations from low to high energy. With $h_Q = 0.35J$, $J = 0.18$ meV and $m \simeq 12\%$, the zero temperature DSF Eq. (4) of H shows that both 1- and 2-strings are confined by the effective field $\mathbf{h}_z$, which plays the same role as that of the staggered field for the confinement in the AFM phase. Accordingly, confined 2-strings exhibit a characteristic M-shaped high-energy continuum that is gapped from the low-energy counterpart of confined 1-strings (Fig. 3**d2**) [38]. The appearance of a "gap" between these two continua reflects the energy cost for the confinement of the 2-strings compared with the deconfined case (Fig. 3**c1,c2**). Both the characteristic gap and the shape of continua can be quantitatively compared between experimental (Fig. 3**d1**) and theoretical results (Fig. 3**d2**), which explicitly confirms the confinement of the Bethe strings of spin chains in YAO. In addition, at zero transfer energy, a series of satellite peaks appear at nQ ($n = 1, 2, \cdots$) in Fig. 3**d2** [38]. This is because the effective field $\mathbf{h}_z$ can connect two Bethe states with momentum difference $\Delta q = Q$ and stabilizes an SDW-ordered ground state. And this ground state has all the Bethe states with momentum being integer times of Q, which makes possible transitions at many different momentum-transfer. Therefore, the satellite peaks only occur at $q = nQ$, which is consistent with the multi-fermion scattering mechanism [22].

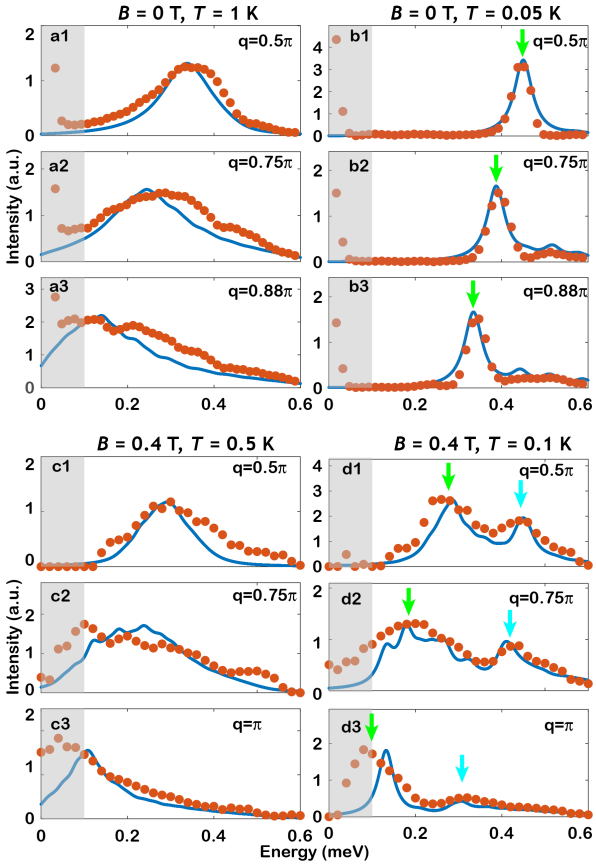

FIG. 4. Comparison of the INS scattering intensity with theoretical calculations. Energy cuts at constant momentum transfers for different magnetic fields and temperatures. Red points and blue lines are results from INS measurements and Bethe-ansatz calculations, respectively. The green and cyan arrows indicate the positions of confined 1-strings and 2-strings, respectively. The INS data in light-gray regions ($\lesssim$ 0.1 meV) are contaminated by elastic line contribution.

The energy cuts at constant momenta resolve the continua and peaks of Bethe strings in Fig. 4. The broad peaks of the 1-string continuum are well captured by theoretical calculations with consideration of thermal fluctuation (Fig. 4**a1-3**). From the AFM to the SDW phase, confined 1-strings (Fig. 4**b1-3**) are suppressed by a magnetic field and give way to the confined 2-strings at high-energy regions (Fig. 4**d1-3**). While in the disordered region at 0.4 T, the confinement effect disappears, and the deconfined 2-strings are hidden inside the 1-string continuum (Fig. 4**c1-3**). Note that the region with energy $\gtrsim$ 0.1 meV, the theoretical results quantitatively agree with the experimental data. Especially, the double peaks in experimental data are evidently confirmed to be the confined 1- and 2-strings (indicated by green and cyan arrows in Fig. 4**d1-3**)

Conclusion. To conclude, we establish a unified phys-

ical picture based on Bethe string to understand spin dynamics in different phases of YAO. In the AFM phase, excitations of confined 1-strings are predominant in the whole dynamical spectrum, while confined 2-strings take control of the high-energy branch of spin dynamics in the SDW phase. The excellent comparisons between theoretical and experimental results explicitly justify the validity of the Bethe-string-based picture and further confirm the confinement of many-body Bethe strings in real material. Following the picture, it allows a uniform characterization of spin dynamics at different phases of a material, which is beyond the conventional understanding based on static order parameters and low-energy effective theories. Our study may also inspire research on non-integrable magnetic systems, and potentially provides a path toward a more complete understanding of the many-body quantum magnetism.

Acknowledgements. We acknowledge R. Yu for helpful discussion and R. Jiang for assistance in plotting Fig.1**a**. This work at Shanghai Jiao Tong University is supported by National Natural Science Foundation of China No. 12274288 and the Innovation Program for Quantum Science and Technology Grant No. 2021ZD0301900 and the Natural Science Foundation of Shanghai with grant No. 20ZR1428400 (J.Y. and J.W.). Work at Oak Ridge National Laboratory (ORNL) was supported by the U.S. Department of Energy (DOE), Office of Science, Basic Energy Sciences, Materials Science and Engineering Division. We thank J. Keum for assistance with X-ray Laue measurements. S. E. N. acknowledges financial support from innovation program under Marie Skodowska-Curie Grant No. 884104. This research used resources at the Spallation Neutron Source, a DOE Office of Science User Facility operated by the Oak Ridge National Laboratory. X-ray Laue measurements were conducted at the Center for Nanophase Materials Sciences (CNMS) (CNMS2019-R18) at ORNL, which is a DOE Office of Science User Facility.

* stanislav.nikitin@psi.ch
† wujd@sjtu.edu.cn

[1] F. Bloch, Zeitschrift fr Physik **61**, 206 (1930).
[2] T. Holstein and H. Primakoff, Phys. Rev. **58**, 1098 (1940).
[3] M. Karabach, G. Mller, H. Gould, and J. Tobochnik, Comput. Phys. **11**, 36 (1997).
[4] M. Jimbo and T. Miwa, *Algebraic Analysis of Solvable Lattice Models* (American Mathematical Society, 1995).
[5] J.-S. Caux, J. Mossel, and I. P. Castillo, J. Stat. Mech.: Theory Exp. **2008**, P08006 (2008).
[6] I. P. Castillo, arXiv:2005.10729 [cond-mat] (2020).
[7] J.-S. Caux and R. Hagemans, J. Stat. Mech.: Theory Exp. **2006**, P12013 (2006).
[8] M. Mourigal, M. Enderle, A. Klpperpieper, J.-S. Caux, A. Stunault, and H. M. Rnnow, Nat. Phys. **9**, 435 (2013).
[9] M. Karbach, K. Hu, and G. Muller, arXiv:cond-mat/0008018 (2000).
[10] H. Bethe, Zeitschrift fr Physik **71**, 205 (1931).
[11] M. Takahashi, Prog. Theor. Phys. **46**, 401 (1971).
[12] M. Gaudin, Phys. Rev. Lett. **26**, 1301 (1971).
[13] M. Takahashi and M. Suzuki, Prog. Theor. Phys. **48**, 2187 (1972).
[14] M. Takahashi, *Thermodynamics of One-Dimensional Solvable Models* (Cambridge University Press, 1999).
[15] W. Yang, J. Wu, S. Xu, Z. Wang, and C. Wu, Phys. Rev. B **100**, 184406 (2019).
[16] Z. Wang, J. Wu, W. Yang, A. K. Bera, D. Kamenskyi, A. T. M. N. Islam, S. Xu, J. M. Law, B. Lake, C. Wu, and A. Loidl, Nature **554**, 219 (2018).
[17] Z. Wang, M. Schmidt, A. Loidl, J. Wu, H. Zou, W. Yang, C. Dong, Y. Kohama, K. Kindo, D. I. Gorbunov, S. Niesen, O. Breunig, J. Engelmayer, and T. Lorenz, Phys. Rev. Lett. **123**, 067202 (2019).
[18] A. K. Bera, J. Wu, W. Yang, R. Bewley, M. Boehm, J. Xu, M. Bartkowiak, O. Prokhnenko, B. Klemke, A. T. M. N. Islam, J. M. Law, Z. Wang, and B. Lake, Nat. Phys. **16**, 625 (2020).
[19] M. Kohno, Phys. Rev. Lett. **102**, 037203 (2009).
[20] L. S. Wu, S. E. Nikitin, Z. Wang, W. Zhu, C. D. Batista, A. M. Tsvelik, A. M. Samarakoon, D. A. Tennant, M. Brando, L. Vasylechko, M. Frontzek, A. T. Savici, G. Sala, G. Ehlers, A. D. Christianson, M. D. Lumsden, and A. Podlesnyak, Nat. Commun. **10**, 698 (2019).
[21] A. Podlesnyak, S. E. Nikitin, and G. Ehlers, Journal of Physics: Condensed Matter **33**, 403001 (2021), publisher: IOP Publishing.
[22] S. E. Nikitin, S. Nishimoto, Y. Fan, J. Wu, L. S. Wu, A. S. Sukhanov, M. Brando, N. S. Pavlovskii, J. Xu, L. Vasylechko, R. Yu, and A. Podlesnyak, Nat. Commun. **12**, 3599 (2021).
[23] Y. Fan, J. Yang, W. Yu, J. Wu, and R. Yu, Phys. Rev. Research **2**, 013345 (2020).
[24] S.-i. Tomonaga, Prog. Theor. Phys. **5**, 544 (1950).
[25] J. M. Luttinger, Phys. Rev. **119**, 1153 (1960).
[26] A. Luther and I. Peschel, Phys. Rev. B **12**, 3908 (1975).
[27] O. A. Starykh and L. Balents, Phys. Rev. B **89**, 104407 (2014).
[28] F. H. L. Essler, A. M. Tsvelik, and G. Delfino, Phys. Rev. B **56**, 11001 (1997).
[29] G. Ehlers, A. Podlesnyak, J. L. Niedziela, E. B. Iverson, and P. E. Sokol, Rev. Sci. Instrum. **82**, 085108 (2011).
[30] G. Ehlers, A. Podlesnyak, and A. I. Kolesnikov, Rev. Sci. Instrum. **87**, 093902 (2016).
[31] O. Arnold, J. C. Bilheux, J. M. Borreguero, A. Buts, S. I. Campbell, L. Chapon, M. Doucet, N. Draper, R. F. Leal, M. A. Gigg, *et al.*, Nucl. Instrum. Methods Phys. Res. Sect. A **764**, 156 (2014).
[32] R. A. Ewings, A. Buts, M. D. Le, J. van Duijn, I. Bustinduy, and T. G. Perring, Nucl. Instrum. Methods Phys. Res. Sect. A **834**, 3132 (2016).
[33] M. Klanjšek, M. Horvatić, S. Krämer, S. Mukhopadhyay, H. Mayaffre, C. Berthier, E. Canévet, B. Grenier, P. Lejay, and E. Orignac, Phys. Rev. B **92**, 060408 (2015).
[34] J. W. Negele and H. Orland, *Quantum Many-Particle Systems* (Perseus Books, 1988).
[35] P. M. Chaikin and T. C. Lubensky, *Principles of Condensed Matter Physics* (Cambridge University Press, 1995).

[36] Y. Zhu, *Modern Techniques for Characterizing Magnetic Materials* (Springer, Boston, MA, 2005).

[37] F. Franchini, *An Introduction to Integrable Techniques for One-Dimensional Quantum Systems*, Vol. 940 (Springer, Cham, 2017).

[38] See Supplemental Material, for details of truncated string state space method, and additional calculation results and comparisons.

[39] Z. Wang, J. Wu, S. Xu, W. Yang, C. Wu, A. K. Bera, A. T. M. N. Islam, B. Lake, D. Kamenskyi, P. Gogoi, H. Engelkamp, N. Wang, J. Deisenhofer, and A. Loidl, Phys. Rev. B **94**, 125130 (2016).

[40] A. K. Bera, B. Lake, F. H. L. Essler, L. Vanderstraeten, C. Hubig, U. Schollwöck, A. T. M. N. Islam, A. Schneidewind, and D. L. Quintero-Castro, Phys. Rev. B **96**, 054423 (2017).

[41] Q. Faure, S. Takayoshi, S. Petit, V. Simonet, S. Raymond, L.-P. Regnault, M. Boehm, J. S. White, M. Mnsson, C. Regg, P. Lejay, B. Canals, T. Lorenz, S. C. Furuya, T. Giamarchi, and B. Grenier, Nature Physics **14**, 716 (2018).

[42] B. Lake, A. M. Tsvelik, S. Notbohm, D. Alan Tennant, T. G. Perring, M. Reehuis, C. Sekar, G. Krabbes, and B. Bchner, Nat. Phys. **6**, 50 (2010).

[43] L. S. Wu, S. E. Nikitin, M. Brando, L. Vasylechko, G. Ehlers, M. Frontzek, A. T. Savici, G. Sala, A. D. Christianson, M. D. Lumsden, and A. Podlesnyak, Phys. Rev. B **99**, 195117 (2019).

[44] A. Keselman, L. Balents, and O. A. Starykh, Phys. Rev. Lett. **125**, 187201 (2020).